Quaternary Science Reviews 328 (2024) 108542

Contents lists available at ScienceDirect

Quaternary Science Reviews

journal homepage: www.elsevier.com/locate/quascirev

On the length and intensity of the West African summer monsoon during the last interglacial African humid period

Xiaoxu Shi [a,b,*], Martin Werner [b,*], Francesco S.R. Pausata [c], Hu Yang [a,b], Jiping Liu [d,a], Roberta D'Agostino [e], Roberto Ingrosso [c], Chaoyuan Yang [a], Qinggang Gao [f,g], Gerrit Lohmann [b]

[a] Southern Marine Science and Engineering Guangdong Laboratory (Zhuhai), Zhuhai, China
[b] Alfred Wegener Institute, Helmholtz Center for Polar and Marine Research, Bremerhaven, Germany
[c] University of Quebec in Montreal, Montreal (QC), Canada
[d] School of Atmospheric Sciences, Sun Yat-sen University, Zhuhai, China
[e] Italian National Research Council, Institute of Atmospheric and Climate Sciences, via per Monteroni Km 1.2, 73100, Lecce, Italy
[f] Ice Dynamics and Paleoclimate, British Antarctic Survey, Cambridge, United Kingdom
[g] Department of Earth Sciences, University of Cambridge, Cambridge, United Kingdom

ARTICLE INFO

Handling Editor: Y. Zhao

Dataset link: https://esgf-node.llnl.gov/search/cmip6/

Dataset link: https://zenodo.org/record/8313516

Keywords:
West African summer monsoon
The last interglacial
Climate modeling
Stable water isotopes
Monsoon onset and withdrawal

ABSTRACT

The increase in summer monsoon precipitation over western Africa during the last interglacial (LIG) relative to the pre-industrial (PI) is well documented, but it is uncertain whether this increase is due to larger rainfall rate alone, an extension of the summer monsoon season or a combination of the two. Due to different orbital configuration, the boreal summer of the LIG was warmer but shorter than the PI, potentially influencing the summer monsoon duration. In this study, we employ a newly developed isotope-enabled climate model, AWI-ESM-wiso to investigate the intensity and length of the West African Summer Monsoon (WASM) for both LIG and PI time periods. Our model results indicate that, despite an intensification in summer insolation and an enhanced hydrological cycle, WASM season in the LIG is 9 days shorter compared to the PI. During the LIG, increased insolation in late spring and early summer strengthens the Saharan heat low (SHL) and its associated sub-systems, facilitating a faster accumulation of potential instability and an earlier WASM onset. However, a substantial earlier withdrawal of the WASM is also detected, driven by an earlier southward shift of insolation maximum. Moreover, our findings are further supported by models participating in the 4th phase of the Paleoclimate Modelling Intercomparison Project (PMIP4).

1. Introduction

The last interglacial, often referred to as Marine Isotope Stage 5e (MIS 5e), is a warm period that occurred approximately 130,000 to 115,000 years ago. This period included a notable wet phase centered around 127,000 years ago (hereafter referred to as LIG). During the LIG, differences in orbital parameters (i.e. eccentricity, obliquity, and precession) caused greater seasonality in the Northern Hemisphere, with warmer summers and colder winters relative to the pre-industrial (PI) period (Lunt et al., 2013; Pfeiffer and Lohmann, 2016). Existing terrestrial archives (Scussolini et al., 2019) and model simulations (Jiang et al., 2015; Nikolova et al., 2012; Shi et al., 2022b) suggest an intensification in monsoon precipitation amount across the majority of the Northern Hemisphere continents in LIG relative to the present-day. As suggested by transient simulations with ocean biogeochemistry and dynamic vegetation, the Northern Hemisphere summer warming as well as the enhanced monsoon circulation in the subtropics foster larger carbon storage during 128-121 ka (Schurgers et al., 2006). Moreover, there is concrete evidence that during the LIG, the Sahara desert was covered by a diversity of plants, lakes and rivers that no longer exist today (Drake et al., 2011; Skonieczny et al., 2015; Larrasoaña et al., 2013), becoming a lush and vibrant landscape that surpassed even the green conditions during the Holocene. This phenomenon, often referred to as the "Green Sahara", might have played a significant role in shaping human evolution (Larrasoaña et al., 2013; Larrasoaña, 2021; Drake et al., 2011), and was attributed to the amplified seasonality in the Northern Hemi-

---

[*] Corresponding authors.
E-mail addresses: shixiaoxu@sml-zhuhai.cn (X. Shi), Martin.Werner@awi.de (M. Werner).

https://doi.org/10.1016/j.quascirev.2024.108542
Received 3 September 2023; Received in revised form 16 January 2024; Accepted 8 February 2024

sphere and a significant northward shift of the monsoon rainfall (e.g. Kowalski et al., 1989; Kutzbach and Otto-Bliesner, 1982; DeMenocal et al., 2012). In turn, the greening of the Sahara can exert important influence on the climate, primarily through changes in surface albedo and their consequential impact on the global energy balance (Schurgers et al., 2007).

In nowadays climate, the summer monsoon in the West Africa begins in late June and lasts until September or early October (Xie et al., 2003; Sultan and Janicot, 2003). The onset stage is marked by a rapid northward shift in rainfall maxima from the Gulf of Guinea coast to the Sahel region. This is accompanied by changes in the relevant components of the monsoon circulation, like the African Easterly Jet (AEJ), namely a notable occurrence of a maximum easterly wind at 600 hPa, and Saharan heat low (SHL), referring to a large-scale area of low pressure, high temperatures, and dry air that typically forms over Sahara in northern Africa. The processes controlling the shift of the rainfall maxima include a sudden northward displacement in the SHL system (Ramel et al., 2006), interaction between topography and monsoon circulation (Sultan and Janicot, 2003), as well as inertial instability that acts to advance the moisture convergence northward (Cook and Vizy, 2006). Moreover, a greater inland moisture advection induced by the SHL dynamics, increased vertical wind shear associated with an enhancement in the low-level westerlies and mid-level AEJ, as well as increased shortwave radiation received at the surface are all important factors that contribute to the onset of the WASM (Sultan and Janicot, 2003). However, it is important to note that different conclusions on mechanism triggering the WASM onset can be potentially dependent on sources of data (e.g., model outputs, observations, re-analyses, etc) that are used in different studies.

Although a large number of studies indicate that the monsoon regions were wetter during LIG than PI, there is a lack of knowledge regarding the onset and termination of the summer monsoon due to the coarse temporal resolution of reconstruction records. Therefore, it is unclear whether the enhanced LIG monsoonal precipitation is due to a larger rainfall rate, an extension of the duration of the summer monsoon or both. Due to precession, summer in the Northern Hemisphere occurred near perihelion (aphelion) in the LIG (PI). Therefore, the boreal summer of the LIG was “warmer” and “shorter” compared to PI, respectively caused by an enhanced Northern Hemisphere insolation and a faster revolution of the Earth around the Sun during boreal summer. A question arises here as how these differences affect the onset, withdrawal, and duration of the LIG summer monsoon. As daily fluctuations in precipitation are not resolved by proxy time series, output from climate models at a daily scale is required for examination of the onset/withdrawal/duration of the paleomonsoon. Since the beginning of the summer monsoon is typically followed by an abrupt increase in precipitation, daily mean or pentad (5-day) mean precipitation is frequently employed to determine the arrival of summer monsoon (Wang et al., 2002; Sultan and Janicot, 2003; Dunning et al., 2016; Pausata et al., 2016; Dallmeyer et al., 2020); however, other fields can also be used, e.g. outgoing longwave radiation (Fontaine et al., 2008; Chenoli et al., 2018; Bhatla et al., 2016) and the low-level zonal wind (Wang et al., 2004; Zhang, 2010). Isotope signals, simulated by isotope-enable climate models, offer an alternate method for studying the onset of the summer monsoon in the Northern Hemisphere (Yang et al., 2012; Tian et al., 2001; Vuille et al., 2005; Risi et al., 2008). In general, an increase in tropical rainfall will lead to a stronger depletion of the stable water isotopic composition of the rainfall (typically expressed as δ^{18}O or δD) due to the so-called “amount effect” (Dansgaard, 1964). Risi et al. (2008) showed that an increase in convective activity across the Sahel coincides with a drop (rise) in δ^{18}O (deuterium excess, defined as dex = δD-8δ^{18}O) in precipitation during the initiation of the Africa monsoon. In addition, a more recent study indicated that the isotope-based method is superior to the precipitation-based method for determining the West African summer monsoon onset (Shi et al., 2023).

Table 1
Boundary conditions in PI and LIG.

Boundary conditions	PI	LIG
CO_2 (ppm)	284.3	275
CH_4 (ppb)	808.2	685
N_2O (ppb)	273	255
Eccentricity	0.016764	0.039378
Obliquity	23.459°	24.040°
Perihelion - 180°	100.33°	275.41°

In the present work, we report the results of two simulations conducted using a newly developed Earth system model equipped with stable water isotope diagnostics (AWI-ESM-wiso) under both LIG and PI boundary conditions. We first report the climatological anomalies in LIG relative to PI in terms of some key atmospheric variables and the rainfall isotope composition. Using the model outputs with a daily temporal resolution, we then investigate the key characteristics of the West African summer monsoon (WASM)’s onset, withdrawal, and hence, the overall duration. To the best of our knowledge, this is the first time monsoon-related processes are examined on a daily timescale for the LIG.

2. Methodology

2.1. Model description

The model used in this study, AWI-ESM-wiso, is a state-of-the-art Earth system model developed at the Alfred Wegener Institute (AWI). The atmospheric component is ECHAM6 (Stevens et al., 2013) which contains a land-surface component known as JSBACH representing dynamic vegetation with two types of bare surface and multiple plant functional types (Reick et al., 2021; Brovkin et al., 2009; Reick et al., 2013). The ice-ocean module of AWI-ESM, i.e. FESOM2.0, employs a multi-resolution dynamical core based on finite volume formulation (Danilov et al., 2017). For atmosphere-ocean coupling, AWI-ESM-wiso employs the OASIS3-MCT coupler (Valcke, 2013) with the use of a regular intermediate grid. Bilinear interpolation is applied between the atmospheric/oceanic grid and the intermediate grid during data exchanges. In AWI-ESM-wiso, three stable water isotope tracers, i.e. $H_2^{16}O$, $H_2^{18}O$, and HDO, have been implemented into all relevant components of the hydrological cycle (Shi et al., 2023). In the absence of a phase transition, these tracers are represented as separate forms of water, described identically to bulk moisture in all aggregate states. Differences between isotope tracers and bulk moisture only occur during processes involving phase transformations. In the ocean, stable water isotopes are considered as passive tracers and equilibrium fractionation only occurs during sea ice changes. The performance of the model in simulating climatic and isotopic variables, as well as the climate-isotope relationship has been validated under pre-industrial and mid-Holocene boundary conditions (Shi et al., 2023).

2.2. Experimental setup

We first conduct an equilibrium experiment representing the year 1850 CE, the reference PI simulation. The initial conditions for the atmosphere in our PI simulation are derived from the Atmospheric Model Intercomparison Project (AMIP) (Roeckner et al., 2004). The ocean model is initialized with the World Ocean Atlas (WOA) climatological temperature and salinity data for the years 1950-2000 (Levitus et al.). The initial isotope composition is defined as $\delta^{18}O = -20‰$; $\delta D = -150‰$ for meteoric waters, whereas $\delta^{18}O = 0‰$; $\delta D = 0‰$ for sea water with respect to the V-SMOW scale. Under the boundary conditions proposed by Otto-Bliesner et al. (2017) (see Table 1 for more detailed information), we run the PI simulation for 1,500 model years with dynamic vegetation. The Plant Functional Types (PFTs) considered in our

Table 2

Starting and end date of angular month in PI and LIG, referencing to today's classical calendar in a no-leap year. Calendar conversion is performed based on a new approach described in Shi et al. (2022a). In this approach, the length of an angular month/season is calculated based on a 30°/90° increment of the true anomaly (i.e., the angle between the perihelion on the major axis of the orbit ellipsoid and the current position of earth), which means that the PI calendar should also be corrected.

Month/Season	PI	LIG
Jan.	02Jan.-30Jan.	26Dec.-27Jan.
Feb.	31Jan.-01Mar.	28Jan.-28Feb.
Mar.	02Mar.-31Mar.	01Mar.-31Mar.
Apr.	01Apr.-01May.	01Apr.-30Apr.
May.	02May.-01Jun.	01May.-29May.
Jun.	02Jun.-02Jul.	30May.-26Jun.
Jul.	03Jul.-02Aug.	27Jun.-24Jul.
Aug.	03Aug.-02Sep.	25Jul.-22Aug.
Sep.	03Sep.-03Oct.	23Aug.-20Sep.
Oct.	04Oct.-02Nov.	21Sep.-21Oct.
Nov.	03Nov.-02Dec.	22Oct.-22Nov.
Dec.	03Dec.-01Jan.	23Nov.-25Dec.
DJFM	03Dec.-31Mar. (119)	23Nov.-31Mar. (129)
JJAS	02Jun.-03Oct. (124)	30May.-20Sep. (114)

PI setup includes evergreen and deciduous trees, rain green and cold shrubs, C3- and C4-type grass, crop and pasture (Fig. S1). We then perform a LIG simulation branching from the last model year of PI but with different orbital parameters and greenhouse gases following Otto-Bliesner et al. (2017), for 1,000 model years. Note that in our LIG experiment, land-use (crop and pasture) is excluded from the PFTs. For both experiments we consider the last 100 years where only modest trends in temperature, salinity and isotope composition in deep ocean are detected. Both experiments are configured on T63L47 grid for the atmosphere, which consists of 47 vertical levels and a global mean spatial resolution of approximately 1.9x1.9 degrees. The ocean component adopts a spatially-variable resolution of up to 25 km over polar regions and 35 km along coastlines and over the equatorial belt.

The performance of AWI-ESM-wiso in simulating the pre-industrial climate and isotopic composition has been evaluated in Shi et al. (2023). As shown in Fig. S2, in general the modeled $\delta^{18}O_p$ values are in good agreement with GNIP database (IAEA, 2018), speleothems (Comas-Bru et al., 2020), and ice core records (WAIS Divide Project Members, 2013; Sundqvist et al., 2014). The isotope composition of sea water produced by our model show great similarity with an assimilation product by Breitkreuz et al. (2018) (Fig. S3). For further details on the model evaluation we refer to Shi et al. (2023).

2.3. Calendar correction

We convert the classical calendar to the angular calendar using the method described in Shi et al. (2022a). The starting and ending dates (referencing to the classical calendar) of each angular month for the two time periods are displayed in Table 2. Using the modern classical calendar can result in erroneous results for temperature anomalies, particularly in JJA and SON, with artificial biases of up to 4 K (Shi et al., 2022a). In the present study, all results regarding the seasonal means are calculated using the angular calendar.

2.4. Definitions of the onset/withdrawal/duration of WASM

The onset date of WASM is defined utilizing both a traditional precipitation-based method (Sultan and Janicot, 2003; Pausata et al., 2016) and a new isotope-based approach as presented in Shi et al. (2023). First, an Empirical Orthogonal Function (EOF) analysis is performed on the daily precipitation over the WASM area (0-40°N, 15°W-20°E) of PI/LIG for the period spanning from March to November (Fig. S4). The latitudinal locations of the first two EOFs maxima are computed to represent the position of the Intertropical Convergence Zone (ITCZ) during the monsoon and pre-monsoon periods. Specifically, the first EOF represents the north location of the ITCZ, while the second EOF represents the south location. For each experiment, we then calculate the time series of precipitation and isotope index (defined as the anomaly between $\delta^{18}O_p$ and deuterium excess in precipitation (dex_p)) at the respective north location averaged over 15°W – 20°E during the period of 1st June to 31st July. The time series is filtered using a running mean analysis to eliminate variability with a period shorter than 10 days. In the precipitation-based approach, the monsoon's onset is defined as the date preceding the largest increase in zonally averages precipitation. Whilst in the isotope-based approach, the onset of WASM is defined as the time when a peak in the isotope index occurs. When multiple peaks are present, further steps are taken to calculate the precipitation trend for each peak over the subsequent 20 days, and the peak that precedes the largest precipitation trend is identified as the onset of the WASM for that particular model year. With respect to the withdrawal of the WASM, our analysis exclusively employs the daily precipitation time series as it provides a clear transition from the rainy season to the dry season. According to Pausata et al. (2016), the withdrawal is identified as the date on which the zonally averaged precipitation at the north latitude falls below 2 mm/day, for at least 20 consecutive days. The monsoon's duration is simply computed as the time interval between its onset and withdrawal.

2.5. Other model data used

We process PI and LIG precipitation data from climate models in the 4th phase of the Paleoclimate Modelling Intercomparison Project (PMIP4) archive to have a further view of the WASM duration. For the purpose of our study, only models providing daily precipitation for both PI and LIG simulations are selected. The models that fulfill our requirement include: AWI-ESM-1-1-LR (Sidorenko et al., 2015; Rackow et al., 2018), CESM2 (Gettelman et al., 2019), EC-Earth3-LR (Zhang et al., 2021), INM-CM4-8 (Volodin et al., 2018), and IPSL-CM6A-LR (Lurton et al., 2020). As the PMIP4 models do not include water isotopes, we employ the precipitation-based method for calculating the WASM onset.

3. Climate and isotope differences between LIG and PI over Africa

The most remarkable difference between LIG and PI in surface air temperature over Africa is a year-round cooling in the tropical areas (Fig. 1a-e). For other regions, we observe an intensification of seasonality (Fig. 1a-e), with a cooling in boreal winter and a warming in boreal summer driven by corresponding anomalies in incoming solar insolation (Fig. S5). During MAM and SON, the insolation change is relatively minor compared to other seasons (Fig. S5). The simulated temperature anomalies in MAM and SON are similar to those in DJF and JJA respectively despite to a lesser extent. The precipitation anomalies, as depicted in Fig. 1f-j, indicate an increase in local precipitation over northern Africa, which finds its greatest expression in JJA, indicating a stronger LIG summer monsoon as well as a northward shift of the tropical convergence zone. The main reason lies on the increased net energy input (NEI, the difference in radiative fluxes between the top-of-atmosphere and the Earth's surface) in the Northern Hemisphere during the LIG compared to the PI. This enhanced NEI, with a magnitude of about 8 W/m^2, results in a significantly amplified hemispheric energy contrast by 6.7 W/m^2. As a consequence, it intensifies the tropical hydrological cycle and shift the tropical convergence zone towards the Northern Hemisphere. Similar mechanism has been applied for the mid-Holocene period (D'Agostino et al., 2019). Our results regarding the anomalies in temperature and precipitation between LIG and PI are consistent with other Earth system models (Otto-Bliesner et al., 2021). However, our model underestimates the wettening in Africa as documented in proxy

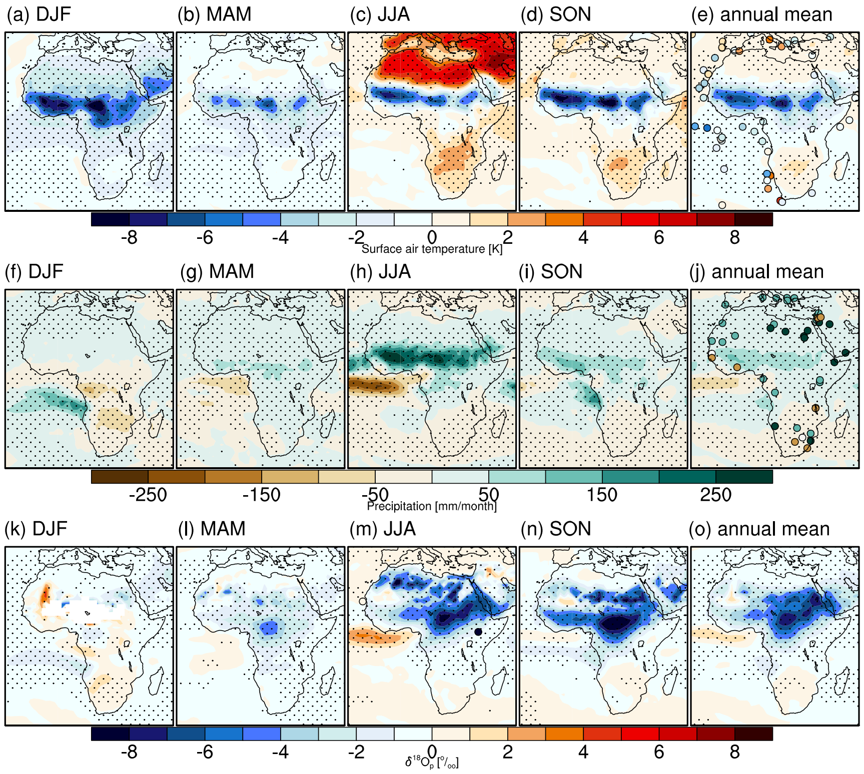

Fig. 1. Simulated anomalies (LIG-PI) of surface air temperature (top), precipitation (middle), and precipitation-weighted $\delta^{18}O_p$ (bottom) for (a,f,k) December to February (DJF), (b,g,l) March-to-May (MAM), (c,h,m) June-to-August (JJA), (d,i,n) September-to-November (SON), and (e,j,o) annual mean. Marked areas have significance levels larger than 95% based on Student's t-test. Circles in (e) represent temperature reconstruction based on Turney and Jones (2010). Circles in (j) represent precipitation reconstruction from Scussolini et al. (2019). Circles in (m) represent $\delta^{18}O_p$ reconstruction from Lupien et al. (2022) and Kuechler et al. (2013).

records (Scussolini et al., 2019). This underestimation is a common issue in Earth system models (Otto-Bliesner et al., 2021). According to Scussolini et al. (2019), mismatches between simulated and reconstructed LIG precipitation have multiple potential sources, for example model deficiencies, inaccuracy in proxy reconstructions and interpretation, as well as insufficient constrains on key boundary conditions in the LIG experiment setup.

The aforementioned differences in surface temperature and precipitation leave considerable imprints on the oxygen-18 composition of precipitation (henceforth denoted by $\delta^{18}O_p$) as shown in Fig. 1k-o. In northern Africa, precipitation is isotopically more depleted as a result of an increase in the precipitation amount (i.e., the "amount effect", Dansgaard (1964)). This phenomenon is most pronounced during the WASM season. Unfortunately, there are very limited isotope records available for Africa for the LIG period. According to a leaf wax isotope record from paleolake sediment cores, the isotopic rainfall values over the Chew Bahir region were significantly more depleted during the LIG than in the PI (Lupien et al., 2022). In addition, another leaf wax record drilled off northwest Africa reveals a slight enrichment in isotope composition (Kuechler et al., 2013) (Fig. 1m).

Consecutive dry days (CDD) and consecutive wet days (CWD) are effective indicators of precipitation extremes, representing the largest number of consecutive days with daily precipitation amounts below and above 1 mm, respectively. Under PI condition, the Sahara experiences an extreme dryness for most of the year, with a mean CDD being more than 250 days for most parts of the Sahara (Fig. 2a). In comparison to PI, a northward extension of summer monsoon and an intensified hydrological cycle in LIG lead to a significant decrease in CDD for the Sahara region (Fig. 2b) by up to 120 days (Fig. 2c). In PI, northern Africa does not experience consecutive rainfall events throughout the year, resulting in a mean CWD of 0 (Fig. 2d). A zero-CWD area is also simulated over northern Africa in the LIG, but much smaller (Fig. 2e). As shown in Fig. 2f, more humid conditions in the LIG lead to a larger CWD for most parts of Africa, particularly the tropical zones. Our findings regarding the differences in CDD and CWD suggest that there are fewer droughts in the Sahara and more intense precipitation over tropical Africa in the LIG than in the PI. Furthermore, we observe a significant increase in the highest 5-day precipitation amount (RX5day) in the LIG WASM region, with anomalies reaching up to 800 mm (Fig. 2g-i). Our results imply a pronounced intensification in both the frequency and magnitude of the heavy precipitation events in LIG.

4. Onset of the West Africa summer monsoon

In our PI (LIG) simulation, the ITCZ locates at 2.8°N (6.5°N) during the pre-monsoon phase, and undergoes a notable shift to 8.4°N (12.1°N) during the onset of the WASM. The ITCZ location during the pre-monsoon/onset phase is determined by calculating the latitude of the maximum precipitation based on the second/first EOF pattern, as described in Section 2.4. Since the length of each month is different in the two time periods under angular calendar, we describe the time of onset/withdrawal with reference to the vernal equinox, which is fixed at March 21st. Base on our model results, the calculated mean onset date for PI using the precipitation-based and isotope-based approach, is 80 and 81 days after the vernal equinox respectively (see also Table 3), with a standard deviation of 14 and 15 days. Our result is in good agreement with observations analyzed in Dansgaard (1964) for the period 1968–1990, which indicate a monsoon onset of June 24 over the West Africa, corresponding to 85 days after the vernal equinox. In the LIG, the onset date for WASM is found to be earlier than PI by 10 days in both methods, with a standard deviation of 10 days for the isotope-based approach and 11 days for the precipitation-based approach. This indicates a consistent trend across both onset definitions for WASM. Moreover, although our model simulates significant variances in the

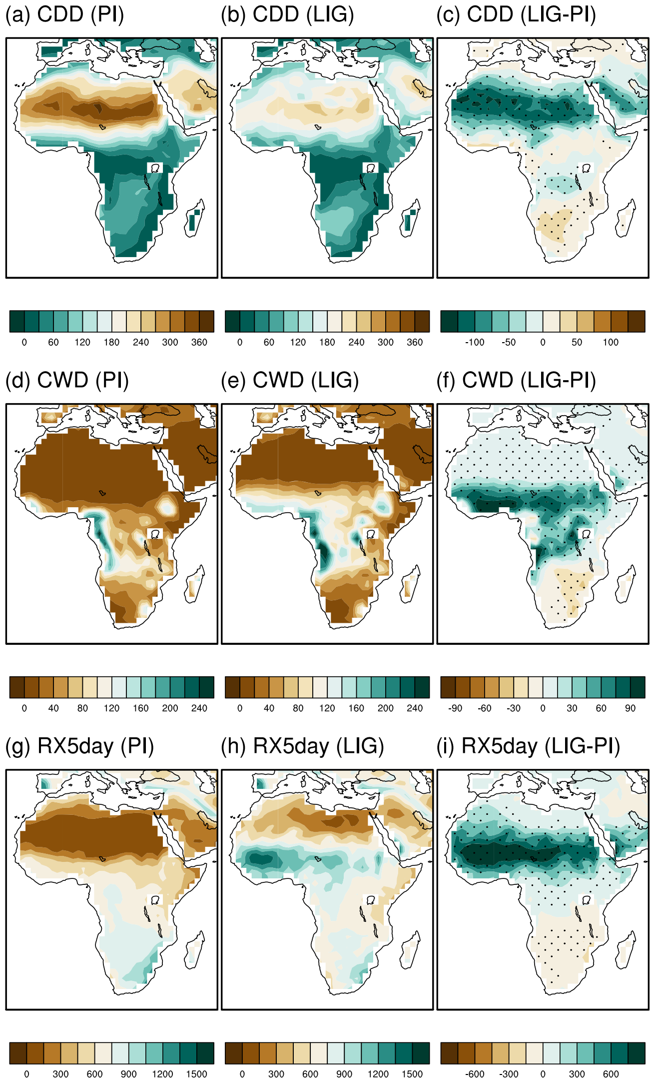

Fig. 2. Simulated consecutive dry days (CCD; top), consecutive wet days (CWD; middle), and the highest five-day precipitation amount (RX5day in mm; bottom) for (a,d,g) PI, (b,e,h) LIG, and (c,f,i) the differences between LIG and PI. Marked areas in (c,f,i) have significance levels larger than 95% based on Student's t-test.

date of WASM onset, the anomaly in the WASM onset between the two experiments is highly significant, with significance levels of over 99% based on Student's t test.

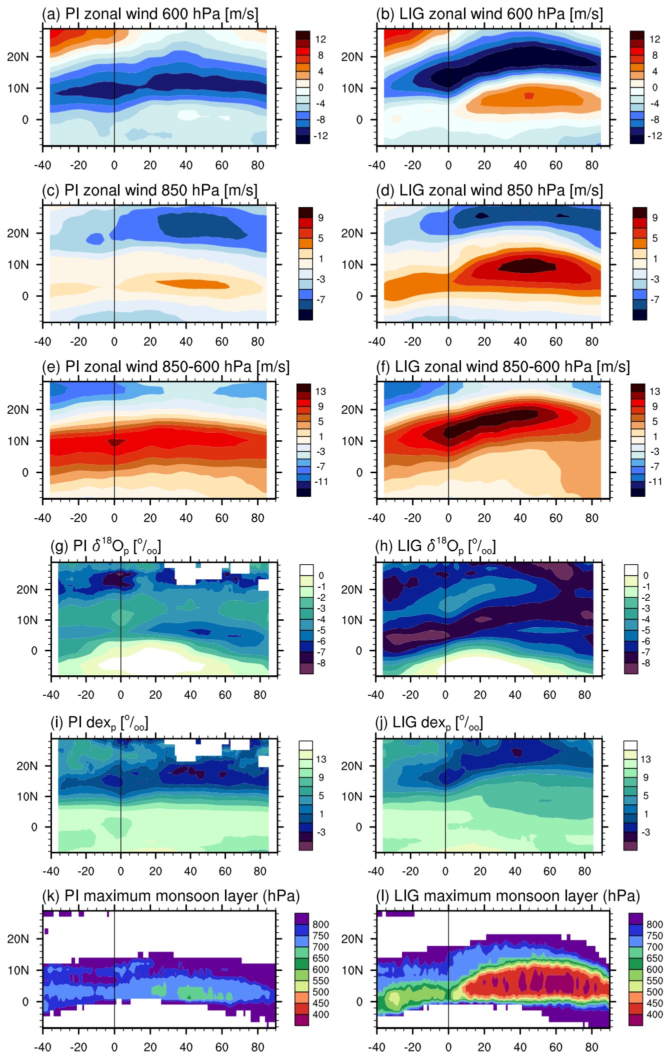

Fig. 3. Simulated composite time–latitude diagram of (a,b) 600 hPa zonal wind (eastward positive), (c,d) 850 hPa zonal wind (westerlies positive), (e,f) zonal wind anomaly between 850 hPa and 600 hPa (westerlies positive), (g,h) $\delta^{18}O_p$, (i,j) deuterium excess in precipitation averaged over 15°W-20°E, and (k,l) the pressure of top monsoon layer under (a,c,e,g,i,k) PI and (b,d,f,h,j,l) LIG climate conditions, filtered with high frequency variability (period less than 10 days) removed. X-axis represents the time shift from the onset date (t0, black lines).

4.1. Processes associated with the WASM onset

In Fig. 3 we depict some of the key features in zonal winds before and after onset of WASM by using composite time-latitude diagrams averaged over the longitudinal range of 15°W-20°E, with the monsoon onset date (t0) for each year being the respective reference date. To ensure accuracy, we restrict our analysis to model years that exhibit comparable onset dates as determined by both the precipitation-based and isotope-based techniques, with a maximum deviation of 3 days between the two methods. The AEJ at 600 hPa is prominently driven by the meridional circulation of the SHL (Thorncroft and Blackburn, 1999). The northerly returning flow at mid-levels associated with the heat low system fosters an easterly acceleration due to planetary vorticity advection (Thorncroft and Blackburn, 1999). Hence, the strength of AEJ can serve as a reliable proxy for the intensity of the SHL. During PI, the AEJ intensifies from 40 days before onset (t0-40) to onset (t0), with its center located at 8.5°N (Fig. 3a). An intensification in AEJ is also observed for LIG but in conjunction with a northward progression from 10°N to 12.5°N (Fig. 3b). This is in agreement with previous studies suggesting an enhancement in SHL prior to the WASM onset (e.g., Sultan and Janicot, 2003). Moreover, we observe an enhancement of the AEJ in LIG compared to PI. This can be attributed to the increased Northern Hemisphere insolation that results in amplified heating over northern Africa. As a consequence, the SHL zone gets warmer than the equatorial regions. This amplified tropical-to-equator temperature gradient gives rise to an easterly flow aloft, which is more pronounced in the LIG than in the PI. Following the onset, a significant displacement in the position of the AEJ is observed from 12.5°N to 20°N during the LIG period, indicating a northward movement of the SHL and the Inter-tropical front (ITF). Conversely, a comparatively less pronounced shift in the AEJ is identified during the PI era.

At 850 hPa, the westerly zonal wind decreases from t0-30 to t0 in the latitude band 0-15°N in both simulations (Fig. 3c,d), followed by an increasing trend that characterizes the monsoon enhancement, with maximal westerlies being observed 40-50 days after the WASM onset. These changes of the zonal winds at 600 hPa and 850 hPa indicate a rise in the vertical wind shear, with the maximum magnitude identified at t0 along 8.5°N in PI (Fig. 3e). According to Sultan and Janicot (2003),

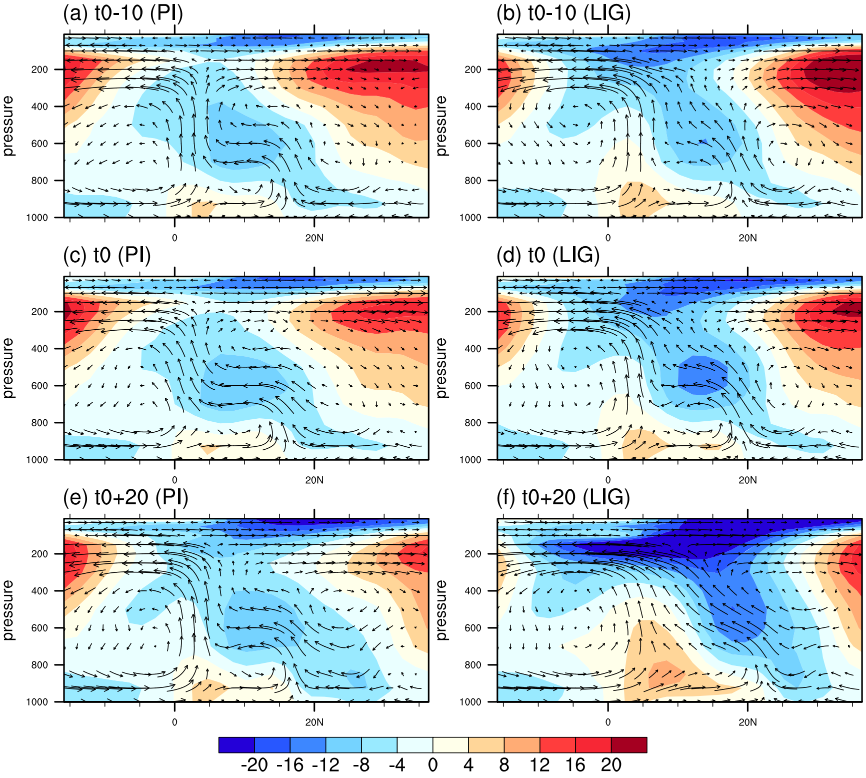

Fig. 4. Composite pressure–latitude cross sections of the atmospheric circulation averaged over 15°W-20°E by using as the WASM onset (t0) as reference date for each year: (a,b) at t0-10, (c,d) at t0, and (e,f) at t0+20. The meridional-vertical circulation is represented by streamlines, shaded areas depict zonal wind (positive values for westerlies). (a,c,e) are for PI and (b,d,e) are for LIG. Units: m/s.

such change is due to a strengthening in AEJ and the SHL-driven anticyclonic circulation in mid-levels. The maximal vertical wind shear at t0, along with a strong inland moisture advection led by the low level westerlies (Fig. 3e,f), contribute to an increase in local potential instability, which is advantageous for the establishment of the summer monsoon regime. An intriguing contrast between PI and LIG is the development of vertical wind shear following the arrival of WASM. In PI, the wind shear reduces after t0, associated with released inertial instability, consistent with the results based on modern observations (e.g., Sultan and Janicot, 2003). In contrast, during LIG the strong vertical shear in zonal winds persists and at the same time propagates from 12°N at t0 to as far north as 18°N at t0+50 (Fig. 3f). The composite time–lat diagrams of zonal winds as shown in Fig. 3a,c,e exhibit good consistency with present-day reanalysis data for the time period of 1968–1990 (Sultan and Janicot, 2003). Nevertheless, during the monsoon mature phase, our PI simulation reveals maximum low-level westerly winds within 0-5°N, whereas the reanalysis data indicate a more northward location (5-10°N).

Fig. 4 illustrates the meridional cross section of the atmospheric circulation associated with the establishment of the WASM, for three specific time-steps: 10 days before onset (t0-10), onset (t0) and 20 days after onset (t0+20). At t0-10, the SHL transverse circulation disturbs the Hadley-type circulation at low-to-middle levels (Fig. 4a,b). Associated with the SHL dynamics, a dry convection occurs between 15-20°N at low levels in both PI and LIG. A deep convection site can be found around 5°N near the surface, accompanied by local westerly winds. Another key feature is the presence of AEJ around 600 hPa within 5-15°N. Compared to PI, the LIG AEJ is more intensified and has a northward displacement. AEJ becomes stronger at t0, which is especially evident in the LIG (Fig. 4d). At t0+20, in the LIG the surface to middle atmosphere between 0-20°N are dominated by monsoonal westerly winds (Fig. 4f), indicating a significant expansion of deep convection in both horizontal and vertical directions after onset. It also implies an elimination of the AEJ at its southern flank, as in PI the prevailing wind pattern in this region remains easterlies (Fig. 4e). Moreover, compared to PI, the AEJ intensifies at its northern flank, indicating a northward shift. Such phenomenon is also simulated for the mid-Holocene AEJ (e.g., Rachmayani et al., 2015; Patricola and Cook, 2007).

4.2. Isotopic signatures associated with the WASM onset

Here we examine the primary characteristics of $\delta^{18}O_p$ and deuterium excess in precipitation (hereinafter dex$_p$) in relation to the beginning date of the WASM (Fig. 3g,h,i,j). During the PI, the start of WASM is accompanied by a peak in $\delta^{18}O_p$ and a corresponding minimum value in dex$_p$ within the latitudinal range of 10-15°N. Following the onset, the monsoon precipitation experiences a depletion in $\delta^{18}O_p$, which is accompanied by a temporary increase in dex$_p$. Our result aligns with the event-based measurements obtained from the region of Niamey (Risi et al., 2008). The detected rise in dex$_p$ and decline in $\delta^{18}O_p$ subsequent to the onset of WASM are due to reduced re-evaporation of falling rain as the atmosphere becomes more humid (Dansgaard, 1964). Variances in $\delta^{18}O_p$ can also be accounted for by the amount effect. In addition, our LIG experiment exhibits a discernible northward migration of the isotope gradient during the time interval of t0 to t0+18, followed by a decrease in $\delta^{18}O_p$ and a temporary increase in dex$_p$.

5. Withdrawal of the West Africa summer monsoon

Both our PI and LIG experiments indicate a growth and a meridional expansion of the monsoon system from initial to mature phase of the WASM (Fig. 3k,l). This enhancement of monsoon can be well estimated via the top of the monsoon layer. Following Lamb (1983), the top of the monsoon layer is defined as the pressure level where the zonal wind component equals zero, going from westerly downward to easterly upward. In comparison to the PI scenario where the top of

Table 3
Onset, withdrawal, and duration of the West African Summer Monsoon for the pre-Industrial, last interglacial period, and the difference between these two time periods across different models. For the onset and withdrawal, the units are “days after the vernal equinox”, while the units for the duration are “days”.

Model	Onset			Withdrawal			Duration		
	PI	LIG	LIG-PI	PI	LIG	LIG-PI	PI	LIG	LIG-PI
AWIESM2.1-wiso	90	80	-10	203	184	-19	113	104	-9
AWIESM-1-1-LR	89	79	-10	199	192	-7	110	113	+3
CESM2	94	88	-6	205	192	-13	111	104	-7
EC-Earth3-LR	83	80	-3	224	204	-20	141	124	-17
INM-CM4-8	92	79	-13	224	199	-25	132	120	-12
IPSL-CM6A-LR	101	95	-6	231	201	-30	130	106	-24

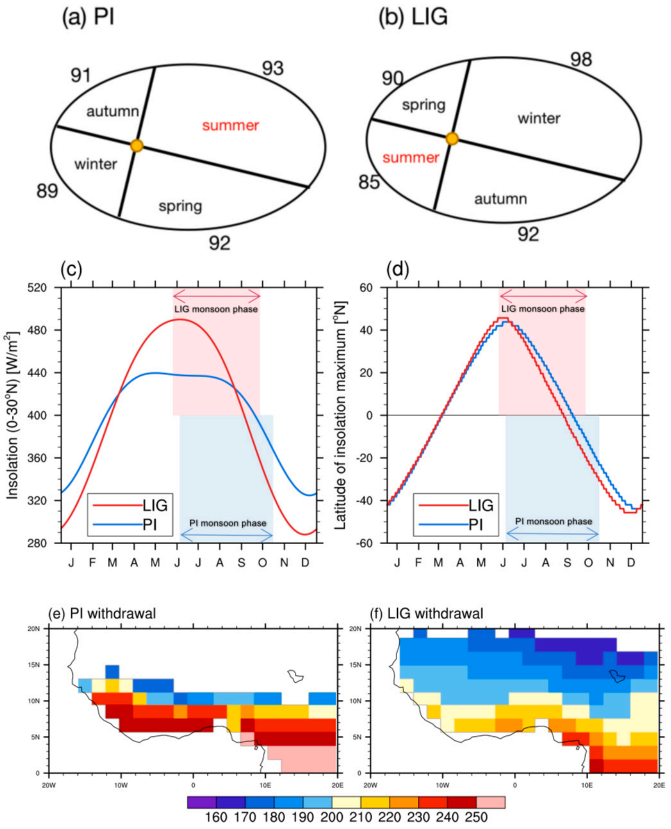

Fig. 5. (a,b) Lengths of Northern Hemisphere seasons for (a) PI and (b) LIG. Units: day. (c) Average incoming insolation over 0-30°N for both PI and LIG. Units: W/m^2 (d) Latitude of insolation maximum for both PI and LIG. Units: °N. Blue and red shading shows the duration of WASM in PI and LIG respectively. (e,f) Withdrawal date of all grid boxes within the WASM domain for (a) PI and (b) LIG. Units: days after the vernal equinox.

the monsoon layer remains below 700 hPa, in the LIG simulation, the monsoon system is significantly deeper, extending up to 400 hPa. This deepening primarily arises due to a larger energy input associated with increased insolation during northern summer (Fig. 5c). A question arises here whether the larger inertia of the LIG monsoon system could potentially cause a delayed withdrawal of the WASM relative to PI, which could overshadow the impact of the earlier southward movement of the insolation maximum (Fig. 5d)?

The withdrawal of WASM suggested by our model is 203 (184) days after the vernal equinox for PI (LIG), implying an earlier occurrence by 19 days in LIG compared to PI (see also Table 3). The mean duration of the WASM is therefore 9 days shorter in the LIG. Our result regarding the PI WASM withdrawal date is consistent with observations for the time period of 1979-2004 Dalu et al. (2009), which reveal that the WASM terminates in the second week of October (i.e., 201-208 days after the vernal equinox). To gain a more comprehensive view, we also calculate the termination date for each grid box within the WASM domain. For the purposes of this study, the WASM domain is defined as the region within 0-40°N and 15°W-20°E, with a precipitation anomaly greater than 2 mm/day between JJAS and DJFM, as outlined by D’Agostino et al. (2019). An evident meridional gradient can be seen in Fig. 5e,f, where the withdrawal of WASM is observed to occur earlier in the northern regions and later in the southern regions in both PI and LIG, fundamentally driven by the movement of the insolation maximum as well as the spatial changes in moisture supply. Another intriguing feature from Fig. 5e,f is that, the monsoon retreat in the LIG experiment occurs significantly earlier than in the PI experiment across the WASM domain. The difference is particularly pronounced over southern regions, exceeding one month. This change can be attributed to the southward migration of the insolation maximum that occurred earlier in the LIG. Moreover, as shown in Fig. S6, our model result indicates a faster southward retreat of WASM in LIG relative to PI. This is mainly due to the reduced subtropical insolation during the course of monsoon withdrawal (Fig. 5c). Our result underscores the significant influence of the magnitude and latitudinal shift of insolation on WASM termination, which surpasses the impacts from the larger inertia of the LIG monsoon system.

6. PMIP4 results on the WASM duration

Additionally, we analyze the PMIP4 models that provide daily precipitation for both PI and LIG experiments, and compare the results with AWIESM-wiso. For each model, we calculate the date of onset and withdrawal based on its respective north location of ITCZ (see Section 2.4 for more details). As indicated in Table 3, all models consistently show an earlier occurrence in both onset and withdrawal of the WASM in the LIG relative to PI. Except AWI-ESM-1-1-LR which shows a 3-day extension in the LIG WASM season, all other models reveal a shortened length in LIG WASM compared to PI. In particular, the withdrawal of WASM simulated by IPSL-CM6A-LR is 30 days earlier in the LIG than in the PI, dominating a reduced WASM duration by as many as 24 days. In comparison to the IPSL-CM6A-LR result, less pronounced shortening in WASM duration is found in CESM2 (by 7 days), INM-CM4-8 (by 12 days), EC-Earth3-LR (by 17 days), and in our model AWIESM-wiso (by 9 days). Moreover, we do not find any notable correlation between the WASM onset and withdrawal and the north ITCZ location.

7. Discussion and conclusions

In the present work we present the results of two equilibrium simulations carried out under PI and LIG boundary conditions with the use of a newly-established Earth System model, labeled AWI-ESM-wiso, which incorporates water isotope diagnostics. Consistent with other coupled models, our simulations show a rise in precipitation, along with a decrease in isotopic composition of precipitation across northern

Africa. The intensification of LIG WASM precipitation amount relative to PI has been extensively investigated through various studies utilizing both model simulations (e.g., Otto-Bliesner et al., 2021; Herold and Lohmann, 2009) and proxy records (e.g., Scussolini et al., 2019). It is so far not known whether the LIG WASM increase in precipitation is linked to a change in the rate of monsoonal rainfall, a lengthening of the monsoon season, or a combination of the two. However, due to the inadequate temporal resolution of proxy-based records, daily fluctuations of paleo-precipitation remain unresolved, resulting in a dearth of information concerning the initiation and withdrawal of the past WASM. The present work aims to address the aforementioned gap by analyzing these processes linked to the WASM in both PI and LIG.

Following the Earth's seasonal revolution around the sun, the WASM conventionally starts in June and terminates in late September or early October. Differences in orbital parameters led to an increased speed of Earth's revolution in the summer semester during the LIG as compared to the PI era. This resulted in a shortening in Northern Hemisphere summer time by 8 days for JJA and 10 days for JJAS (Fig. 5a,b). During the boreal autumn, there is a notable shift in the maximal insolation from the Northern to the Southern Hemisphere. This shift occurs earlier in the LIG period compared to the PI (Fig. 5d, Fig. S5c), which has the potential to influence the southward migration of the ITCZ and the duration of the WASM (i.e., the duration effect of the insolation). On the other hand, during the LIG the Northern Hemisphere received more insolation in boreal spring and summer relative to PI (Fig. 5c), which could facilitate a larger tropical to equatorial temperature gradient in the upper troposphere, thus help to trigger and maintain an active state of the summer monsoon (i.e., the magnitude effect of the insolation).

Our model results indicate an earlier occurrence in both the onset (by 10 days) and the termination (by 19 days) of LIG WASM compared to PI, resulting in a shortening in the LIG WASM season by 9 days. The Saharan heat low (SHL), an area of high surface temperatures and low surface pressures, is an important trigger for the WASM onset (Lavaysse et al., 2009; Sultan and Janicot, 2003; Ramel et al., 2006; Sijikumar et al., 2006). It exists throughout the year and takes place where insolation is high and evaporation is low. The typical Hadley circulation at low- to-mid atmospheric levels is disturbed by the SHL. According to Sultan and Janicot (2003), the monsoon onset follows an intensification of SHL that favors a more intensified intrusion of dry, subsiding air from the north, which inhibits deep convection at first. Then, SHL-related inland moisture advection together with a strong vertical wind shear increase the potential instability, break the convection inhibition and finally trigger the establishment of the monsoon system, as well as a Hadley-type circulation. This coincides with the well-established Rotunno et al. (1988) theory. A more recent study proposed that a stronger SHL can inhibit Sahel rainfall by advecting midtropospheric warm and dry air into the precipitation maximum (Shekhar and Boos, 2017). Another study suggests that the WASM onset is induced by a northward shift of the SHL (Ramel et al., 2006). This shift, as pointed out by Lavaysse et al. (2009), is to a first order driven by the northward displacement of insolation maximum. Our results of both PI and LIG experiments indicate that the WASM establishes when the AEJ and vertical zonal wind shear enhances and reach a temporary peak value, and these phenomena are associated with an intensification of the SHL. One key impacting factor for SHL is the gradual intensification of solar radiation in the northern tropics, which increases thermal and moisture contrasts between the Guinea Gulf and the tropical Atlantic, thereby contributing to the establishment of the SHL (Janicot et al., 2011). As indicated by Lavaysse et al. (2009), the meridional displacement of the SHL is significantly influenced by the maximum surface solar radiation. In addition, Plumb and Hou (1992) demonstrates that the monsoon circulation develops when the rate of subtropical heating surpasses a specific threshold. Therefore, the earlier formation of WASM during the LIG is fundamentally driven by increased insolation in northern summer which contributes to more intense deepening of the SHL system in the pre-monsoonal season. This amplification is instrumental in establishing the summer monsoon circulation by enhancing the vertical zonal wind shear and inland moisture transport. Moreover, the earlier termination of WASM in the LIG highlights the prevailing influence of the southward shift of insolation maximum.

CRediT authorship contribution statement

X. Shi developed the original idea for this study, performed the model simulations and data analysis, and wrote the initial draft. M. Werner and G. Lohmann led the project and provided supervision throughout the research. FSR. Pausata, H. Yang, J. Ping, R. D'Agostino, R. Ingrosso, C. Yang, and Q. Gao contributed valuable discussions and assisted with the data analysis. All authors made substantial contributions to the writing of the paper.

Declaration of competing interest

The authors declare that they have no known competing financial interests or personal relationships that could have appeared to influence the work reported in this paper.

Data availability

The PMIP4 model data used in this study can be accessed from https://esgf-node.llnl.gov/search/cmip6/. The model output used in this study can be accessed via https://zenodo.org/record/8313516.

Acknowledgements

The present study is supported by the National Natural Science Foundation of China (NSFC) (grant no. 42206256), Southern Marine Science and Engineering Guangdong Laboratory (Zhuhai) (grant no. 313023003) and German Federal Ministry of Education and Science (BMBF) PalMod II WP 3.3 (grant no. 01LP1924B). QG has received funding from the European Union's Horizon 2020 research and innovation programme under the Marie Sklodowska-Curie (grant no. 955750). The simulations were conducted on the high performance computing system of the Deutsche Klimarechenzentrum (DKRZ).

Appendix A. Supplementary material

Supplementary material related to this article can be found online at https://doi.org/10.1016/j.quascirev.2024.108542.

References

Bhatla, R., Ghosh, S., Mandal, B., Mall, R., Sharma, K., 2016. Simulation of Indian summer monsoon onset with different parameterization convection schemes of RegCM-4.3. Atmos. Res. 176, 10–18.

Breitkreuz, C., Paul, A., Kurahashi-Nakamura, T., Losch, M., Schulz, M., 2018. A dynamical reconstruction of the global monthly mean oxygen isotopic composition of seawater. J. Geophys. Res., Oceans 123, 7206–7219.

Brovkin, V., Raddatz, T., Reick, C.H., Claussen, M., Gayler, V., 2009. Global biogeophysical interactions between forest and climate. Geophys. Res. Lett. 36.

Chenoli, S.N., Jayakrishnan, P., Samah, A.A., Hai, O.S., Mazuki, M.Y.A., Lim, C.H., 2018. Southwest monsoon onset dates over Malaysia and associated climatological characteristics. J. Atmos. Sol.-Terr. Phys. 179, 81–93.

Comas-Bru, L., Rehfeld, K., Roesch, C., Amirnezhad-Mozhdehi, S., Harrison, S.P., Atsawawaranunt, K., Ahmad, S.M., Brahim, Y.A., Baker, A., Bosomworth, M., Breitenbach, S.F.M., Burstyn, Y., Columbu, A., Deininger, M., Demény, A., Dixon, B., Fohlmeister, J., Hatvani, I.G., Hu, J., Kaushal, N., Kern, Z., Labuhn, I., Lechleitner, F.A., Lorrey, A., Martrat, B., Novello, V.F., Oster, J., Pérez-Mejías, C., Scholz, D., Scroxton, N., Sinha, N., Ward, B.M., Warken, S., Zhang, H., members, S.W.G., 2020. Sisalv2: a comprehensive speleothem isotope database with multiple age–depth models. Earth Syst. Sci. Data 12, 2579–2606. https://doi.org/10.5194/essd-12-2579-2020. https://essd.copernicus.org/articles/12/2579/2020/.

Cook, K.H., Vizy, E.K., 2006. Coupled model simulations of the West African monsoon system: twentieth- and twenty-first-century simulations. J. Climate 19, 3681–3703.

D'Agostino, R., Bader, J., Bordoni, S., Ferreira, D., Jungclaus, J., 2019. Northern hemisphere monsoon response to mid-Holocene orbital forcing and greenhouse gas-induced global warming. Geophys. Res. Lett. 46, 1591–1601.

Dallmeyer, A., Claussen, M., Lorenz, S.J., Shanahan, T., 2020. The end of the African humid period as seen by a transient comprehensive Earth system model simulation of the last 8000 years. Clim. Past 16, 117–140.

Dalu, G.A., Gaetani, M., Meneguzzo, F., Crisci, A., Maracchi, G., Guarnieri, F., Capecchi, V., 2009. The hydrological onset and withdrawal index (HOWI) for the West Africa monsoon. Theor. Appl. Climatol. 5–4.

Danilov, S., Sidorenko, D., Wang, Q., Jung, T., 2017. The finite-volume sea ice–ocean model (FESOM2). Geosci. Model Dev. 10, 765–789.

Dansgaard, W., 1964. Stable isotopes in precipitation. Tellus 16, 436–468.

DeMenocal, P.B., Tierney, J.E., et al., 2012. Green Sahara: African humid periods paced by Earth's orbital changes. Nat. Educ. Knowl. 3, 12.

Drake, N.A., Blench, R.M., Armitage, S.J., Bristow, C.S., White, K.H., 2011. Ancient watercourses and biogeography of the Sahara explain the peopling of the desert. Proc. Natl. Acad. Sci. 108, 458–462.

Dunning, C.M., Black, E.C., Allan, R.P., 2016. The onset and cessation of seasonal rainfall over Africa. J. Geophys. Res., Atmos. 121, 11–405.

Fontaine, B., Louvet, S., Roucou, P., 2008. Definition and predictability of an OLR-based West African monsoon onset. Int. J. Climatol., J. R. Meteorol. Soc. 28, 1787–1798.

Gettelman, A., Hannay, C., Bacmeister, J., Neale, R., Pendergrass, A., Danabasoglu, G., Lamarque, J.-F., Fasullo, J., Bailey, D., Lawrence, D., et al., 2019. High climate sensitivity in the community Earth system model version 2 (CESM2). Geophys. Res. Lett. 46, 8329–8337.

Herold, M., Lohmann, G., 2009. Eemian tropical and subtropical African moisture transport: an isotope modelling study. Clim. Dyn. 33, 1075–1088.

IAEA, 2018. International atomic energy agency/world meteorological organization, global network of isotopes in precipitation, the GNIP database. Available at https://nucleus.iaea.org/wiser.

Janicot, S., Caniaux, G., Chauvin, F., De Coëtlogon, G., Fontaine, B., Hall, N., Kiladis, G., Lafore, J.-P., Lavaysse, C., Lavender, S.L., et al., 2011. Intraseasonal variability of the West African monsoon. Atmos. Sci. Lett. 12, 58–66.

Jiang, D., Tian, Z., Lang, X., 2015. Mid-Holocene global monsoon area and precipitation from PMIP simulations. Clim. Dyn. 44, 2493–2512.

Kowalski, K., Van Neer, W., Bocheński, Z., Młynarski, M., Rzebik-Kowalska, B., Szyndlar, Z., Gautier, A., Schild, R., Close, A.E., Wendorf, F., 1989. A last interglacial fauna from the eastern Sahara. Quat. Res. 32, 335–341.

Kuechler, R., Schefuß, E., Beckmann, B., Dupont, L., Wefer, G., 2013. Nw African hydrology and vegetation during the last glacial cycle reflected in plant-wax-specific hydrogen and carbon isotopes. Quat. Sci. Rev. 82, 56–67.

Kutzbach, J., Otto-Bliesner, B., 1982. The sensitivity of the African-Asian monsoonal climate to orbital parameter changes for 9000 years BP in a low-resolution general circulation model. J. Atmos. Sci. 39, 1177–1188.

Lamb, P.J., 1983. West African water vapor variations between recent contrasting Subsaharan rainy seasons. Tellus, Ser. A Dyn. Meteorol. Oceanogr. 35, 198–212.

Larrasoaña, J.C., 2021. A review of West African monsoon penetration during green Sahara periods; implications for human evolution and dispersals over the last three million years. Oxford Open Clim. Change 1, kgab011.

Larrasoaña, J.C., Roberts, A.P., Rohling, E.J., 2013. Dynamics of green Sahara periods and their role in hominin evolution. PLoS ONE 8, e76514.

Lavaysse, C., Flamant, C., Janicot, S., Parker, D.J., Lafore, J.-P., Sultan, B., Pelon, J., 2009. Seasonal evolution of the West African heat low: a climatological perspective. Clim. Dyn. 33, 313–330.

Levitus, S., Locarnini, R.A., Boyer, T.P., Mishonov, A.V., Antonov, J.I., Garcia, H.E., Baranova, O.K., Zweng, M.M., Johnson, D.R., Seidov, D., 2010. World ocean atlas 2009.

Lunt, D., Abe-Ouchi, A., Bakker, P., Berger, A., Braconnot, P., Charbit, S., Fischer, N., Herold, N., Jungclaus, J.H., Khon, V., et al., 2013. A multi-model assessment of last interglacial temperatures. Clim. Past 9, 699–717.

Lupien, R.L., Russell, J.M., Pearson, E.J., Castañeda, I.S., Asrat, A., Foerster, V., Lamb, H.F., Roberts, H.M., Schäbitz, F., Trauth, M.H., et al., 2022. Orbital controls on eastern African hydroclimate in the Pleistocene. Sci. Rep. 12, 3170.

Lurton, T., Balkanski, Y., Bastrikov, V., Bekki, S., Bopp, L., Braconnot, P., Brockmann, P., Cadule, P., Contoux, C., Cozic, A., et al., 2020. Implementation of the CMIP6 forcing data in the IPSL-CM6A-LR model. J. Adv. Model. Earth Syst.

Nikolova, I., Yin, Q., Berger, A., Singh, U., Karami, M., 2012. The last interglacial (Eemian) climate simulated by LOVECLIM and CCSM3. Clim. Past Discuss. 8.

Otto-Bliesner, B., Braconnot, P., Harrison, S., Lunt, D., Abe-Ouchi, A., Albani, S., Bartlein, P., Capron, E., Carlson, A., Dutton, A., et al., 2017. The PMIP4 contribution to CMIP6–part 2: two interglacials, scientific objective and experimental design for Holocene and last interglacial simulations. Geosci. Model Dev. 10, 3979–4003.

Otto-Bliesner, B.L., Brady, E.C., Zhao, A., Brierley, C.M., Axford, Y., Capron, E., Govin, A., Hoffman, J.S., Isaacs, E., Kageyama, M., et al., 2021. Large-scale features of last interglacial climate: results from evaluating the lig127k simulations for the coupled model intercomparison project (CMIP6)–paleoclimate modeling intercomparison project (PMIP4). Clim. Past 17, 63–94.

Patricola, C.M., Cook, K.H., 2007. Dynamics of the West African monsoon under mid-Holocene precessional forcing: regional climate model simulations. J. Climate 20, 694–716.

Pausata, F.S., Messori, G., Zhang, Q., 2016. Impacts of dust reduction on the northward expansion of the African monsoon during the green Sahara period. Earth Planet. Sci. Lett. 434, 298–307.

Pfeiffer, M., Lohmann, G., 2016. Greenland ice sheet influence on last interglacial climate: global sensitivity studies performed with an atmosphere–ocean general circulation model. Clim. Past, 1313–1338.

Plumb, R.A., Hou, A.Y., 1992. The response of a zonally symmetric atmosphere to subtropical thermal forcing: threshold behavior. J. Atmos. Sci. 49, 1790–1799.

Rachmayani, R., Prange, M., Schulz, M., 2015. North African vegetation–precipitation feedback in early and mid-Holocene climate simulations with CCSM3-DGVM. Clim. Past 11, 175–185.

Rackow, T., Goessling, H.F., Jung, T., Sidorenko, D., Semmler, T., Barbi, D., Handorf, D., 2018. Towards multi-resolution global climate modeling with ECHAM6-FESOM. Part ii: climate variability. Clim. Dyn. 50, 2369–2394.

Ramel, R., Gallée, H., Messager, C., 2006. On the northward shift of the West African monsoon. Clim. Dyn. 26, 429–440.

Reick, C., Raddatz, T., Brovkin, V., Gayler, V., 2013. Representation of natural and anthropogenic land cover change in MPI-ESM. J. Adv. Model. Earth Syst. 5, 459–482.

Reick, C.H., Gayler, V., Goll, D., Hagemann, S., Heidkamp, M., Nabel, J.E., Raddatz, T., Roeckner, E., Schnur, R., Wilkenskjeld, S., 2021. JSBACH 3-the land component of the MPI Earth System Model: documentation of version 3.2.

Risi, C., Bony, S., Vimeux, F., Descroix, L., Ibrahim, B., Lebreton, E., Mamadou, I., Sultan, B., 2008. What controls the isotopic composition of the African monsoon precipitation? Insights from event-based precipitation collected during the 2006 AMMA field campaign. Geophys. Res. Lett. 35.

Roeckner, E., Brokopf, R., Esch, M., Giorgetta, M., Hagemann, S., Kornblueh, L., Manzini, E., Schlese, U., Schulzweida, U., 2004. The atmospheric general circulation model ECHAM5 part II: sensitivity of simulated climate to horizontal and vertical resolution.

Rotunno, R., Klemp, J.B., Weisman, M.L., 1988. A theory for strong, long-lived squall lines. J. Atmos. Sci. 45, 463–485.

Schurgers, G., Mikolajewicz, U., Gröger, M., Maier-Reimer, E., Vizcaíno, M., Winguth, A., 2006. Dynamics of the terrestrial biosphere, climate and atmospheric CO2 concentration during interglacials: a comparison between Eemian and Holocene. Clim. Past 2, 205–220.

Schurgers, G., Mikolajewicz, U., Gröger, M., Maier-Reimer, E., Vizcaíno, M., Winguth, A., 2007. The effect of land surface changes on Eemian climate. Clim. Dyn. 29, 357–373.

Scussolini, P., Bakker, P., Guo, C., Stepanek, C., Zhang, Q., Braconnot, P., Cao, J., Guarino, M.-V., Coumou, D., Prange, M., et al., 2019. Agreement between reconstructed and modeled boreal precipitation of the last interglacial. Sci. Adv. 5, eaax7047.

Shekhar, R., Boos, W.R., 2017. Weakening and shifting of the Saharan shallow meridional circulation during wet years of the West African monsoon. J. Climate 30, 7399–7422.

Shi, X., Werner, M., Krug, C., Brierley, C.M., Zhao, A., Igbinosa, E., Braconnot, P., Brady, E., Cao, J., d'Agostino, R., et al., 2022a. Calendar effects on surface air temperature and precipitation based on model-ensemble equilibrium and transient simulations from PMIP4 and PACMEDY. Clim. Past 18, 1047–1070.

Shi, X., Werner, M., Wang, Q., Yang, H., Lohmann, G., 2022b. Simulated mid-Holocene and last interglacial climate using two generations of AWI-ESM. J. Climate 35, 4211–4231.

Shi, X., Cauquoin, A., Lohmann, G., Jonkers, L., Wang, Q., Yang, H., Sun, Y., Werner, M., 2023. Simulated stable water isotopes during the mid-Holocene and pre-industrial using AWI-ESM-2.1-wiso. Geosci. Model Dev. Discuss. 2023, 1–39.

Sidorenko, D., Rackow, T., Jung, T., Semmler, T., Barbi, D., Danilov, S., Dethloff, K., Dorn, W., Fieg, K., Gößling, H.F., et al., 2015. Towards multi-resolution global climate modeling with ECHAM6–FESOM. Part I: model formulation and mean climate. Clim. Dyn. 44, 757–780.

Sijikumar, S., Roucou, P., Fontaine, B., 2006. Monsoon onset over Sudan-Sahel: simulation by the regional scale model MM5. Geophys. Res. Lett. 33.

Skonieczny, C., Paillou, P., Bory, A., Bayon, G., Biscara, L., Crosta, X., Eynaud, F., Malaizé, B., Revel, M., Aleman, N., et al., 2015. African humid periods triggered the reactivation of a large river system in western Sahara. Nat. Commun. 6, 1–6.

Stevens, B., Giorgetta, M., Esch, M., Mauritsen, T., Crueger, T., Rast, S., Salzmann, M., Schmidt, H., Bader, J., Block, K., et al., 2013. Atmospheric component of the MPI-M earth system model: ECHAM6. J. Adv. Model. Earth Syst. 5, 146–172.

Sultan, B., Janicot, S., 2003. The West African monsoon dynamics. Part II: the "preonset" and "onset" of the summer monsoon. J. Climate 16, 3407–3427.

Sundqvist, H.S., Kaufman, D.S., McKay, N., Balascio, N., Briner, J., Cwynar, L., Sejrup, H., Seppä, H., Subetto, D., Andrews, J., et al., 2014. Arctic Holocene proxy climate database–new approaches to assessing geochronological accuracy and encoding climate variables. Clim. Past 10, 1605–1631.

Thorncroft, C., Blackburn, M., 1999. Maintenance of the African easterly jet. Q. J. R. Meteorol. Soc. 125, 763–786.

Tian, L., Masson-Delmotte, V., Stievenard, M., Yao, T., Jouzel, J., 2001. Tibetan Plateau summer monsoon northward extent revealed by measurements of water stable isotopes. J. Geophys. Res., Atmos. 106, 28081–28088.

Turney, C.S., Jones, R.T., 2010. Does the Agulhas current amplify global temperatures during super-interglacials? J. Quat. Sci. 25, 839–843.

Valcke, S., 2013. The OASIS3 coupler: a European climate modelling community software. Geosci. Model Dev. 6, 373–388.

Volodin, E.M., Mortikov, E.V., Kostrykin, S.V., Galin, V.Y., Lykossov, V.N., Gritsun, A.S., Diansky, N.A., Gusev, A.V., Iakovlev, N.G., Shestakova, A.A., et al., 2018. Simulation of the modern climate using the INM-CM48 climate model. Russ. J. Numer. Anal. Math. Model. 33, 367–374.

Vuille, M., Werner, M., Bradley, R., Keimig, F., 2005. Stable isotopes in precipitation in the Asian monsoon region. J. Geophys. Res., Atmos. 110.

WAIS Divide Project Members, 2013. Onset of deglacial warming in West Antarctica driven by local orbital forcing. Nature 500, 440–444.

Wang, B., et al., 2002. Rainy season of the Asian–Pacific summer monsoon. J. Climate 15, 386–398.

Wang, B., Zhang, Y., Lu, M., 2004. Definition of South China Sea monsoon onset and commencement of the East Asia summer monsoon. J. Climate 17, 699–710.

Xie, P., Janowiak, J.E., Arkin, P.A., Adler, R., Gruber, A., Ferraro, R., Huffman, G.J., Curtis, S., 2003. Gpcp pentad precipitation analyses: an experimental dataset based on gauge observations and satellite estimates. J. Climate 16, 2197–2214.

Yang, X., Yao, T., Yang, W., Xu, B., He, Y., Qu, D., 2012. Isotopic signal of earlier summer monsoon onset in the Bay of Bengal. J. Climate 25, 2509–2516.

Zhang, H., 2010. Diagnosing Australia-Asian monsoon onset/retreat using large-scale wind and moisture indices. Clim. Dyn. 35, 601–618.

Zhang, Q., Berntell, E., Axelsson, J., Chen, J., Han, Z., De Nooijer, W., Lu, Z., Li, Q., Zhang, Q., Wyser, K., et al., 2021. Simulating the mid-Holocene, last interglacial and mid-Pliocene climate with EC-Earth3-LR. Geosci. Model Dev. 14, 1147–1169.